Assessment of Drone-based Surface Flow Observations

Flavia Tauro *[1], Andrea Petroselli[2], and Ettore Arcangeletti[2]

[1]*Dipartimento per l'Innovazione nei sistemi Biologici, Agroalimentari e Forestali, University of Tuscia, Viterbo 01100, Italy.*
[2]*Dipartimento di scienze e tecnologie per l'Agricoltura, le Foreste, la Natura e l'Energia, University of Tuscia, Viterbo 01100, Italy.*

September 22, 2015

Abstract

Remote surface flow observations are crucial for improving the comprehension of hydrological phenomena. A recent advancement in remote hydrological measurements involves the use of drones for generating surface flow velocity field maps through Large Scale Particle Image Velocimetry (LSPIV). In this work, we perform a comparative analysis of drone-based LSPIV with fixed implementations. Quantitative indices are introduced to test the efficiency of the techniques with respect to measurement accuracy, sensitivity to the transit of tracers, and platform mobility. Experimental findings support drone-based observations in outdoor settings. Specifically, measurements from the aerial platform are more sensitive to the transit of tracers and closer to benchmark values than traditional LSPIV implementations. Future work should aim at improving the stability of the aerial platform and mitigating the effects of tracer scarcity.

*flavia.tauro@unitus.it; Corresponding author

1 Introduction

Surface flow measurements are crucial for understanding the organization of natural waters and predicting hydrological phenomena. However, the availability of accurate observations is hindered by practical difficulties (Hrachowitz et al., 2013; McDonnell et al., 2007). For instance, flow observations in difficult-to-access environments are challenging, and current measurement procedures are often intrusive and highly user-assisted (Buchanan and Somers, 1969). Such drawbacks are partially addressed by optical techniques, such as Large Scale Particle Image Velocimetry (LSPIV), which entails the use of digital video acquisition systems to construct velocity maps of surface flows.

LSPIV is a remote surface flow measurement system that enables potentially continuous characterization of water bodies based on digital image acquisition from locations placed outside the flow current (Fujita et al., 1997; Bradley et al., 2002). Directly based on classical particle image velocimetry (PIV), which is typically used in fluid mechanics laboratories to estimate the instantaneous flow velocity of seeded fluids (Adrian, 1991, 2005; Raffel et al., 2007), this technique has found several applications in hydrological sciences. For instance, it has been instrumental to estimate hydrodynamic features in natural water bodies (Hauet et al., 2009) and flow discharge and patterns in riverine and limnological environments (Creutin et al., 2003; Jodeau et al., 2008; Kantoush and Schleiss, 2009). LSPIV does not require either physical sampling or the presence of operators (Gunawan et al., 2012; Kantoush et al., 2011), and allows for safely monitoring extended channel reaches in varying flow regimes, ranging from heavy floods to low flows (Bechle et al., 2012; Tsubaki et al., 2011). For instance, in a recent application (LeBoursicaud et al., 2015), videos captured from an amateur are utilized to estimate flow discharge during an extreme event.

LSPIV implementations include digital cameras installed at a distant position and inclined with respect to the water surface and a processing unit to a posteriori analyze images and extract the flow velocity field (Kim et al., 2008; Muste et al., 2008, 2011). Typically, floating material is added onto the water surface to improve visibility. In the absence of externally added material, foam, bubbles, or naturally occurring debris can be used for flow tracing. In the post-analysis phase, images are orthorectified using ground reference points (GRPs) and are assigned metric dimensions (Hauet et al., 2008). After orthorectification, surface flow velocity is estimated by applying a high-speed cross-correlation algorithm on sequences of captured images (Raffel et al., 2007).

According to (Kantoush et al., 2011; Hauet et al., 2008; Kim, 2006), LSPIV measurements are highly sensitive to the surface seeding density, the acquisition of

GRPs, and the process of image orthorectification. In (Tauro et al., 2014), limitations related to image orthorectification and calibration are addressed by developing a portable telescopic apparatus, whereby the camera axis is perpendicular to the water surface and a system of lasers creates reference points in the field of view for image calibration. This apparatus is nonintrusive and inherently thought for installations underneath bridges and boardwalks. However, monitored fields are spatially limited, and can only be varied upon reinstallation of the setup in alternative locations.

Fully remote surface flow observations are achieved in (Pagano et al., 2014; Tauro et al., 2015a,b), where a custom-built and a commercial drones are used for surface flow observations on small scale streams. In the last years, drones have empowered the realm of Earth science with novel observational capabilities. They enable data collection in hostile environments (McGonigle et al., 2008; Shelley et al., 2014) and observations at the large scale (Cohen, 2007; Schiffman, 2014). Among environmental applications, drone technology has been adopted to map drainage networks in glacial environments (Rippin et al., 2015), to study erosion and deposition dynamics (Eltner et al., 2014; Smith and Vericat, 2015), to monitor crop fields (Gago et al., 2015) and coastal wetlands (Klemas, 2015), and to investigate channel reach morphology (Tamminga et al., 2015). Further, low-cost drones have enabled the generation of digital elevation models in impoverished areas (Heimhuber et al., 2015), and have been tested for environmental disaster and flooding sensing (Liu et al., 2015; Luo et al., 2015). In (Pagano et al., 2014; Tauro et al., 2015b), the feasibility of drone-based flow velocimetry is demonstrated through proof-of-concept experiments. Notably, in (Tauro et al., 2015b), the drone hovering accuracy is characterized in an outdoor laboratory, and the platform is then used to yield accurate surface flow maps at sub-meter spatial resolution on the Rio Cordon mountainous stream in the Italian Alps, Italy.

In this work, we build on the promising findings in (Tauro et al., 2015b) to quantitatively assess the performance of drone-based surface flow measurements in outdoor settings against fixed LSPIV implementations. Specifically, the efficacy of surface flow observations from an aerial sensing platform is investigated with respect to traditional LSPIV implementations and the modified portable LSPIV configuration presented in (Tauro et al., 2014) through experiments performed in the Rio Cordon. Data from each experimental configuration are evaluated with respect to: i) the accuracy of velocity estimations with respect to benchmark values; ii) the sensitivity to the transit of tracing material; and iii) the effect of the mobility of the apparatus. In addition, this assessment explores the dependence of the different experimental configurations on the observation time length and on the type of tracer released on the water surface.

The selected experimental site features a high-flow regime, small scale, artificial stream with shallow water depths and incident sunlight. To provide a thorough assessment of the potential of LSPIV-based observations in these challenging settings, in this work, two different locations are selected along the stream. In the first location, surface flow velocities are higher and the water surface is mostly shadowy. In the second location, the water depth is extremely shallow ($2 - 3\,\mathrm{cm}$) and the surface is directly illuminated. Remote surface flow observations are performed from a commercial low cost drone, whereas the portable telescopic system in (Tauro et al., 2014) is utilized for the fixed configurations. Experiments are conducted both with and without tracers. Namely, two classes of floating materials, that is, high-visibility particles and natural debris are deployed in the stream. Further, tests are performed in the absence of added material and using water reflections as tracers to evaluate the influence of tracer visibility on measurement accuracy.

The rest of the paper is organized as follows. In Section 2, the study site and instrumentation are described. Further, details are provided on the experimental campaign, LSPIV analyses, and the quantitative parameters introduced for the assessment. In Section 3, experimental findings from all experimental configurations are reported for each location. In Section 4, results are discussed and advantages and limitations of the illustrated methodologies are presented. Finally, Section 5 is left for concluding considerations and future perspectives.

2 Methodology

2.1 Study Site

Surface flow observations are executed at a gauging station located in the Rio Cordon natural catchment, Italy (Tauro et al., 2012a). The Rio Cordon drains a $7.68\,\mathrm{km}^2$ natural basin located in the Dolomites, Northeastern Italy. This mountainous stream is a tributary of the Fiorentina stream that in turn flows into the Rio Cordevole. The catchment drainage network extends for approximately 19 km at an average slope of 47.85%. The Agenzia regionale per la prevenzione e protezione ambientale del Veneto (A.R.P.A.V.) gauging station is located at 1763 m above sea level and is equipped with water gauges, a coarse sediment grille, and a diversion pool for water and finer material.

Figure 2.1 presents a map view of the gauging station. Experimental observations are conducted at two different locations. A set of tests is executed at the artificially channelled stream reach located in the proximity of the downstream gauge. The selected stream reach is a rectilinear tract with a concrete rectangular section that is

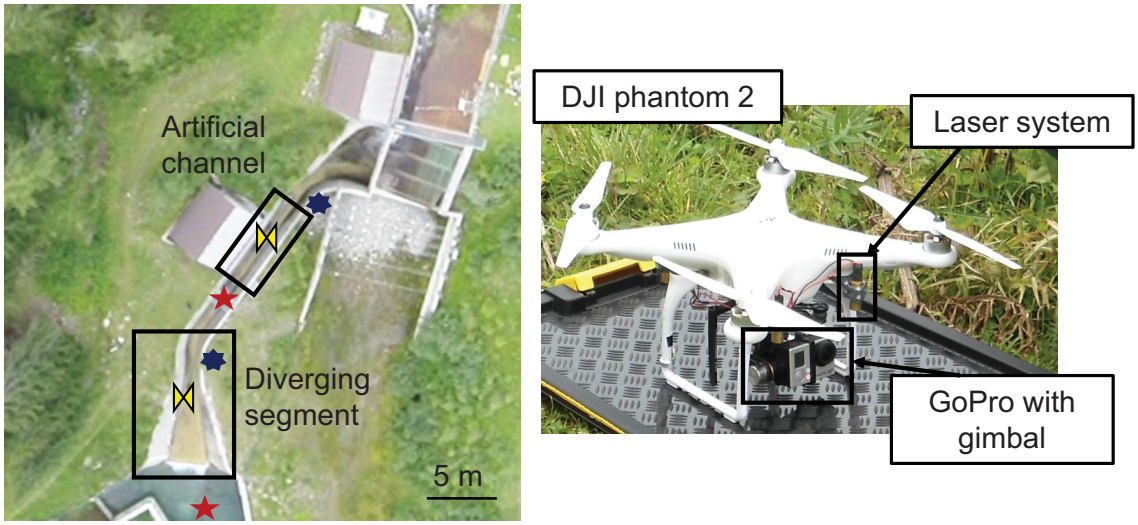

Figure 2.1: Left, aerial view of the study site: solid boxes indicate the locations where surface flow observations are conducted. Red stars indicate the location of the fixed sensing platforms (a boardwalk for the artificial channel and a downstream bridge, not visible in the picture, for the diverging segment), and yellow markers denote the approximate location of the drone. Dark blue markers indicate the locations along the stream banks where tracer deployment occurs. Right, view of the aerial sensing platform. The DJI Phantom 2 features a H3-2D gimbal, a GoPro Hero 3 camera, and a system of four green lasers.

1 m wide and was 11 cm deep at the time of the experiments, as per measurements provided by A.R.P.A.V. Another set of measurements is conducted at the diverging stream segment that spills water into the downstream pool.

2.2 Aerial and fixed sensing platforms

The aerial sensing platform is a DJI Phantom 2 quadrotor (DJI, 2014) mounting a Zenmuse H3-2D gimbal and a GoPro Hero 3 camera oriented with its axis along the perpendicular, see Figure 2.1. The gimbal allows for compensating the drone's vibrations about the pitch and roll axes while minimizing distortions in videos. Remote photometric calibration is enabled through four green lasers (532 nm in wavelength and less than 5 mW in power) installed at the four corners of the fuselage and aligned with the drone's yaw axis. The drone is flown above the artificially channelled stream reach and the divergent stream segment to capture fields of view of approximately $9 \times 5\,\mathrm{m}^2$ and $30 \times 17\,\mathrm{m}^2$, respectively.

Measurements from the drone are compared to observations obtained from fixed LSPIV configurations based on the apparatus in (Tauro et al., 2014). This portable setup features a system of two low power lasers and was initially introduced for remote surface flow monitoring in riverine settings. In the artificially channelled stream, two configurations of the apparatus are tested. In the fixed-ortho configuration, the camera axis is set perpendicular to the water surface to capture a field of view of $5 \times 3\,\mathrm{m}^2$ (corresponding to the lower region of the field of view captured by the drone). In the fixed-inclined observations, the apparatus is set along the vertical on a bridge boardwalk across the downstream section of the field of view captured by the drone. In this case, the camera axis is inclined with respect to the water surface to capture a field of view of $6 \times 6\,\mathrm{m}^2$.

In the diverging stream segment, aerial data are compared to observations from the fixed-inclined configuration. Specifically, the apparatus is located along the vertical on a downstream bridge above the downstream pool, see Figure 2.1, with the camera axis inclined with respect to the water surface. The total field of view captured from this configuration is $17 \times 30\,\mathrm{m}^2$.

2.3 Experimental data acquisition

Table 1 reports the total number of tests executed in the experimental campaign. In the artificially channelled stream, surface flow measurements are conducted by using both high-visibility artificial beads and naturally floating debris, such as leaves. Artificial tracers are in-house fabricated particles synthesized from biocompatible and

Table 1: Synoptic table of the experimental tests performed in the Rio Cordon. At the artificial channel, tests are executed with three experimental configurations, two types of tracers, and in the absence of floating material. At the diverging segment, drone data are compared to videos from the fixed-inclined configuration. Debris and water reflections are therein used as tracers.

Artificial channel			Diverging segment		
Configuration	Tracer	Replicates	Configuration	Tracer	Replicates
Drone	beads	10	Drone	debris	10
	debris	10		–	6
	–	10			
Fixed - ortho	beads	10			
	–	10			
Fixed - inclined	debris	10	Fixed - inclined	debris	10
	–	10		–	6

buoyant children-friendly dough. Surface flow velocity observations based on the use of high-visibility beads have been demonstrated in (Tauro et al., 2012b,c, 2013a,b). Particle size ranges from 0.5 up to 1 cm, and beads are red, yellow, orange, and green in color. The transit of the artificial particles is captured using the drone and the fixed-ortho configuration. Further, natural debris is used as tracer in experiments from the drone and the fixed-inclined configuration.

Due to the larger field of view and the absence of boardwalks, experiments on the diverging segment of the stream are conducted using only the drone and the fixed-inclined configuration (which enables monitoring over larger areas), and deploying natural debris for flow tracing (which can be massively deployed in the stream). To provide a thorough assessment of the performance of optical observations in outdoor settings, LSPIV analyses are also conducted in the absence of tracers for each configuration ("–" in Table 1).

In both locations, the drone captures Full HD videos at 60 Hz frame rate. In the fixed-ortho and fixed-inclined configurations on the artificial channel, the camera captures 1280×720 pixels videos at 60 Hz frame rate. In the fixed-inclined setup on the diverging segment, Full HD images are captured at 30 Hz frame rate.

2.4 Field data analysis

Experimental videos are fish-eye undistorted using the GoPro Studio 2.0 Software. Further, videos are unpacked to extract grayscale images. Images recorded in the

fixed-inclined configuration are orthorectified using landmarks on the stream banks as GRPs. Preliminary analyses are performed to identify the optimal settings for LSPIV processing through the high-speed cross-correlation edPIV software (Gui, 2013). Table 2 reports the adopted LSPIV settings for each experiment illustrated in Table 1. The average time length of the experiments (Obs. time) is also reported in Table 2.

Table 2: Synoptic table of the parameters adopted for LSPIV processing of data captured in the Rio Cordon. Image resolution and frequency are opportunely adjusted for LSPIV analyses. Average observation times (Obs. time) are reported for each set of experiments.

Artificial channel					
	Tracer	Resolution pixels	Frequency Hz	Obs. time s	Int. window pixels
Drone	beads	Full HD	60	0.6	32×32
	debris	Full HD	60	1.1	32×32
	–	Full HD	60	0.8	64×64
Fixed	beads	1280×720	60	0.7	32×32
- ortho	–	1280×720	60	0.8	64×64
Fixed	debris	720×735	20	2.9	32×32
- inclined	–	720×735	20	1.5	32×32
Diverging segment					
	Tracer	Resolution pixels	Frequency Hz	Obs. time s	Int. window pixels
Drone	debris	Full HD	15	2.6	32×32
Drone	–	Full HD	15	2.5	32×32
Fixed	debris	Full HD	30	2.7	64×64
- inclined	–	Full HD	30	2.7	64×64

LSPIV processing is conducted on sequences of images depicting the continuous transit of tracing material in the entire field of view, whereas images displaying the entrance and exit of tracers from the field of view are not considered. Since the amount of artificial beads deployed in the stream is much lower than natural debris, image sequences pertaining to experiments with the beads are on average shorter than experiments with debris.

2.5 Performance evaluation criteria

Surface flow velocity maps are generated by averaging LSPIV velocity estimates in time. In case of experiments with the drone, the imperfect hovering capability of the platform results in non-null velocities at nodes lying outside the stream. To partially mitigate this effect, the average velocity of the nodes lying outside the stream is computed and subtracted by the entire set of velocity values. For each experimental configuration, subareas of the stream consistently captured in each video are identified, and time-averaged profiles of selected cross-sections in the subareas are computed. To assess the effect of the observation time length, velocity maps are generated by considering 30%, 60%, and 100% of the total number of images for each replicate, thus corresponding to 30%, 60%, and 100%, respectively, of the total observation time length.

Benchmark flow velocity for experiments in the artificial channel is obtained using an OTT C2 small current meter. The instrument is set to the time measurement mode, whereby the number of impulses recorded in 10 s are counted and related to flow velocity. The velocity is measured at a cross-section of the stream a few centimeters upstream the subarea selected for comparison. Measurements result in an average velocity of 2.54 m/s at 0.5 m from the right stream bank (that is, in the center of the stream) and at 3 cm underneath the water surface. Such benchmark value is obtained by averaging over three repetitions. Due to impracticalities in using the current meter in the diverging segment of the stream, benchmark velocity is obtained by manually tracking floating objects in images captured from the fixed-inclined configuration. Specifically, average velocities equal to $1.5-1.8$ m/s are found for the central portion of the diverging segment.

To investigate the performance of drone-based and fixed LSPIV, several parameters are introduced and estimated for each experiment. Specifically, the parameters aim at assessing: i) effect of tracers' visibility during the experiments; ii) impact of eventual vibrations of the experimental platforms; iii) consistency among experimental replicates; iv) accuracy of velocity estimates; and v) accuracy in reconstructing the cross-sectional surface flow profile. The effect of tracers' visibility is assessed through the index $Z = N_0/N_{\text{tot}}$, where N_0 indicates the number of nodes presenting velocity values less or equal to 10% the average velocity in the entire time-averaged map, and N_{tot} is the total number of nodes in the map. In the computation, only nodes pertaining to the stream are retained. Low velocity values captured by the parameter N_0 are in general not representative of the actual flow condition; rather, they are typically due to adverse visibility and tracer scarcity.

The stability of the experimental platform is assessed through the index $D = N_{\text{d}}/N_{\text{tot}}$, where N_{d} refers to the number of nodes presenting negative velocity values,

that is, vectors in the opposite direction of flow. In case of fixed configurations, the index D is found to be equal to zero for all experimental replicates and, therefore, in the following, only data captured from the drone are presented. Consistency among experimental replicates is computed through the structural similarity index (SSIM) (Wang et al., 2004). This index is largely used in image analysis to quantify differences between images in terms of luminance, contrast, and structure. In this work, the SSIM is computed on the time-averaged velocity maps obtained for each experimental replicate. The index is estimated by setting the exponents to 0, 0, and 1 to capture only the maps' structural differences (Wang et al., 2004).

The accuracy of LSPIV-based velocity estimates is assayed by comparing the maximum velocity value obtained in subareas captured in each experiment. Indeed, as showed in (Tauro et al., 2014), high percentiles are found to be closer to actual velocity values in natural streams. Maximum velocity values are computed from the time-averaged maps. Further, to evaluate the efficiency of the experimental configurations at detecting the cross-sectional surface flow profile, the range of selected cross-sections laying in the subareas is computed. The range is estimated by generating time-averaged surface flow velocity maps and then selecting nodes pertaining to three cross-sections.

The variability of the performance evaluation parameters with respect to different tracers and the observation time lengths is assessed through one-way analysis of variance. Specifically, the variability of the data sets with regards to tracers is assessed by estimating the p-values on measurements with and without tracers for each configuration. Dependence on the observation time lengths is computed on measurements evaluated for 30%, 60%, and 100% of the image sequences for each experimental configuration. In the following, p values are only reported when statistically significant. Specifically, weak statistical significance is defined when $0.01 < p < 0.05$, and strong statistical significance is set for $p < 0.01$.

3 Results

3.1 Artificial channel

Figure 3.1 reports representative time-averaged velocity maps obtained from the drone (a) and (b), the fixed-ortho (c), and the fixed-inclined (d) configurations. Next to each map, time-averaged profiles are reported for three cross-sections laying in the subarea shared by all configurations, see black rectangle in maps in Figure 3.1. While the maps depict slightly varying fields of view, all of them present similar features, such as the high velocity region enclosed in the shared subarea. To provide

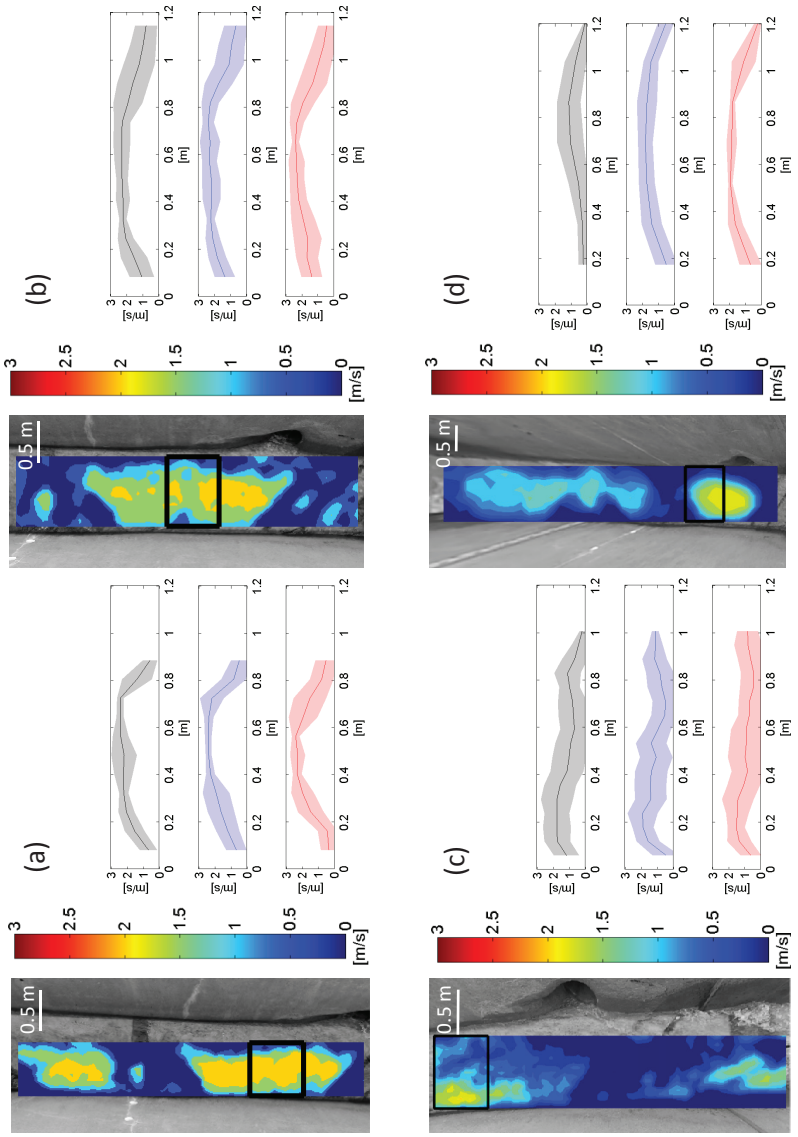

Figure 3.1: Representative surface flow observations for experiments conducted in the artificial channel. (a) Time-averaged surface flow velocity map and cross-sectional profiles generated from drone data and in case of artificial beads as tracers. (b) Time-averaged surface flow velocity map and cross-sectional profiles generated from drone data and in case of natural debris as tracer. (c) Time-averaged surface flow velocity map and cross-sectional profiles generated from the fixed-ortho configuration data and in case of artificial beads as tracers. (d) Time-averaged surface flow velocity map and cross-sectional profiles generated from the fixed-inclined configuration data and in case of natural debris as tracer. Black boxes indicate the subarea shared by all experimental configurations.

a thorough assessment of the tested methodologies, in the following, performance evaluation criteria established in Section 2.5 are computed and presented.

3.1.1 Sensitivity to tracers' transit

Figure 3.2 depicts the index Z for each experimental configuration and type of tracing material. To assess the effect of tracers' visibility on image quality, in Figure 3.2, the index Z is also reported for experiments performed with and without tracers. Black, blue, and red bars correspond to values computed using 30%, 60% and 100% of the total number of images for each experimental replicate. On average, low velocity nodes tend to be more abundant in case of videos from the drone with artificial beads. Further, in case of experiments with the drone, maps based on 30% of the total number of images in the relative sequence present a higher number of low velocities. However, the variability of Z with respect to the observation time length is not statistically significant neither for experiments with the drone nor with fixed configurations. Significant variability is found in case of experiments with the drone with respect to tracers. Specifically, the variability in drone experiments with artificial beads, debris, and without tracers is found strongly statistically significant for each observation time length ($p = 0.0022$, 0.0025, and 0.0023 for 30%, 60%, and 100% of the image sequences, respectively). Indeed, the number of low velocity nodes in the drone configuration without tracers (see first row in Figure 3.2) is much higher than with tracers. In addition, the variability in experiments with the fixed-ortho configuration with respect to tracers is found strongly statistically significant for each observation time length ($p = 0.0021$, 0.0073, and 0.0029 for 30%, 60%, and 100% of the image sequences, respectively). Conversely, variability of data from the fixed-inclined configuration is not found statistically significant with regards to tracers.

3.1.2 Impact of platform's stability

Limitations in the station-keeping capability of the aerial platform are illustrated in Figure 3.3, where the index D is reported for each experimental replicate with the drone. Notably, velocity vectors in the opposite direction of the flow tend to be lower than 20% of the total number of nodes, and are generally smaller upon increasing the observation time. This is due to the fact that the effect of the irregular motion of the drone is averaged in time in case of longer observations. Based on one-way analysis of variance, the variability with respect to the observation time length and tracers is not found statistically significant.

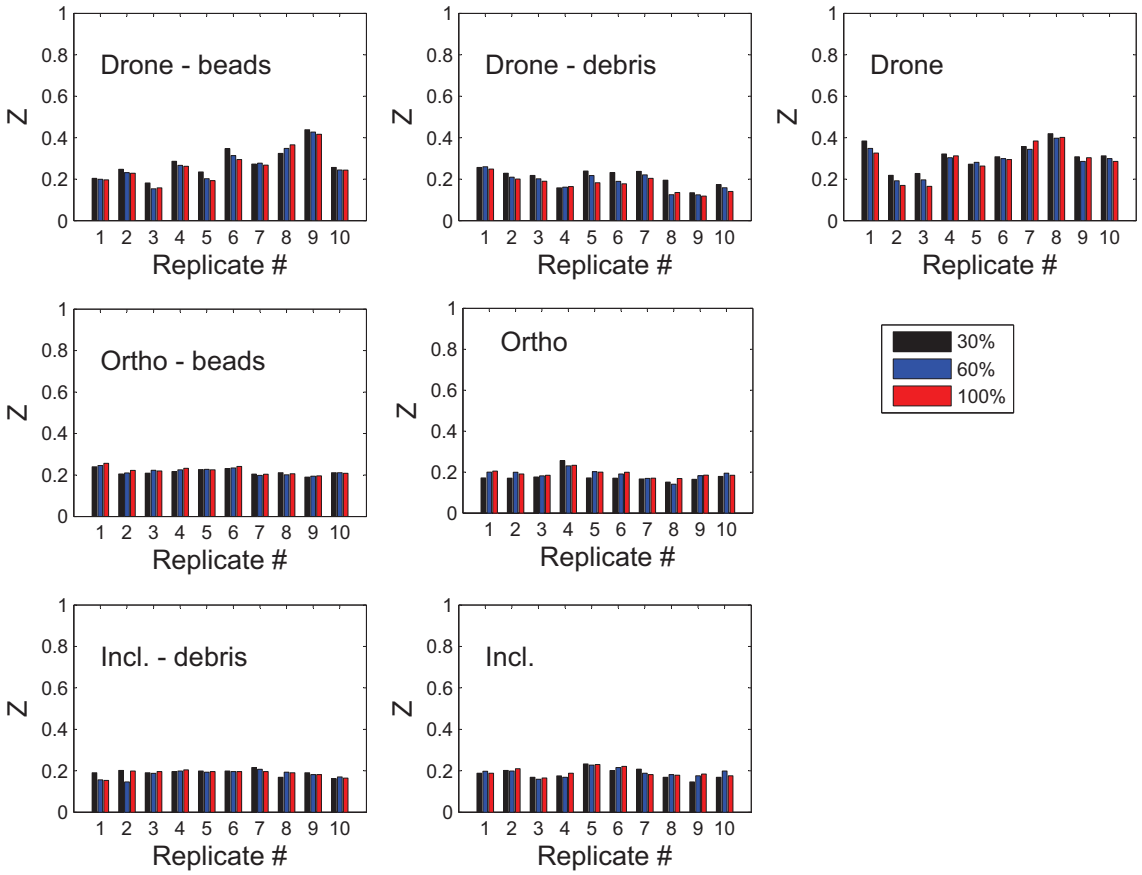

Figure 3.2: Artificial channel: Z values for each experimental condition. In the top row, drone data (Drone) are reported in case of beads, debris, and without tracers. In the central row, data are illustrated for the fixed-ortho configuration (Ortho) in case of beads and without tracers. In the bottom row, data are reported for the fixed-inclined configuration (Incl.) in case of debris and without tracers. For each replicate, Z values are computed considering 30% (black bars), 60% (blue bars), and 100% (red bars) of the image sequences.

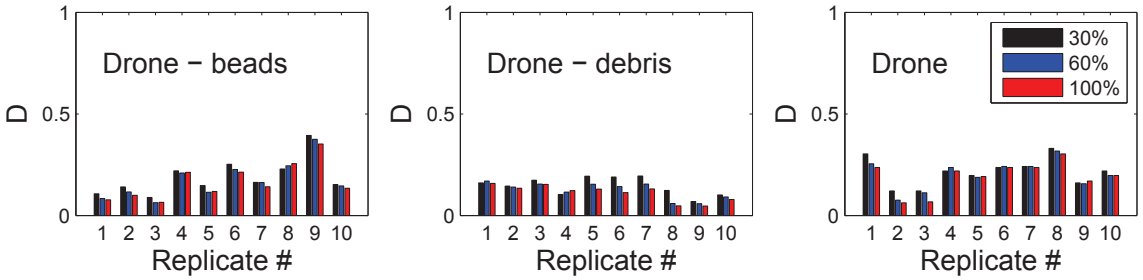

Figure 3.3: Artificial channel: D values for drone-based experiments. For each replicate, D values are computed considering 30% (black bars), 60% (blue bars), and 100% (red bars) of the image sequences.

3.1.3 Experiment repeatability

The similarity index among time-averaged velocity maps is reported in Figure 3.4, whereby the first velocity map is used as reference. Notably, all configurations result in values of the SSIM greater or equal to zero, thus demonstrating that the structure of the maps does not radically vary among different replicates. However, in case of the fixed-inclined configuration and debris, all values of the SSIM are greater than 0.5, thus indicating that maps are highly consistent among replicates. Interestingly, while the structure of the maps generated from drone data (top row in Figure 3.4) do not sensibly vary with respect to the observation time length, a different behavior is found for fixed configurations. Specifically, the SSIM tends to increase with longer observations in case of fixed LSPIV (central and bottom rows in Figure 3.4). Indeed, strong statistical significance ($p = 0.0017$) is found for the inclined-debris data with respect to the observation time length (see bottom left graph in Figure 3.4). Weak statistical significance ($p = 0.0195$) is also observed in the variability of the inclined configuration data (100% of the image sequence) with respect to tracers.

3.1.4 Measurement accuracy

In Figure 3.5, maximum velocity values are reported for subareas indicated in Figure 3.1. For each configuration, the marker indicates the median computed over the experimental replicates. The edges of the box indicate the 25th and 75th percentiles, and the whiskers extend to extreme data points that are not outliers. Interestingly, estimates obtained from drone-beads data tend to be higher than values from alternative experimental settings. Median values from all configurations tend to decrease with longer image sequences (from the top graph to the bottom graph in Figure 3.5).

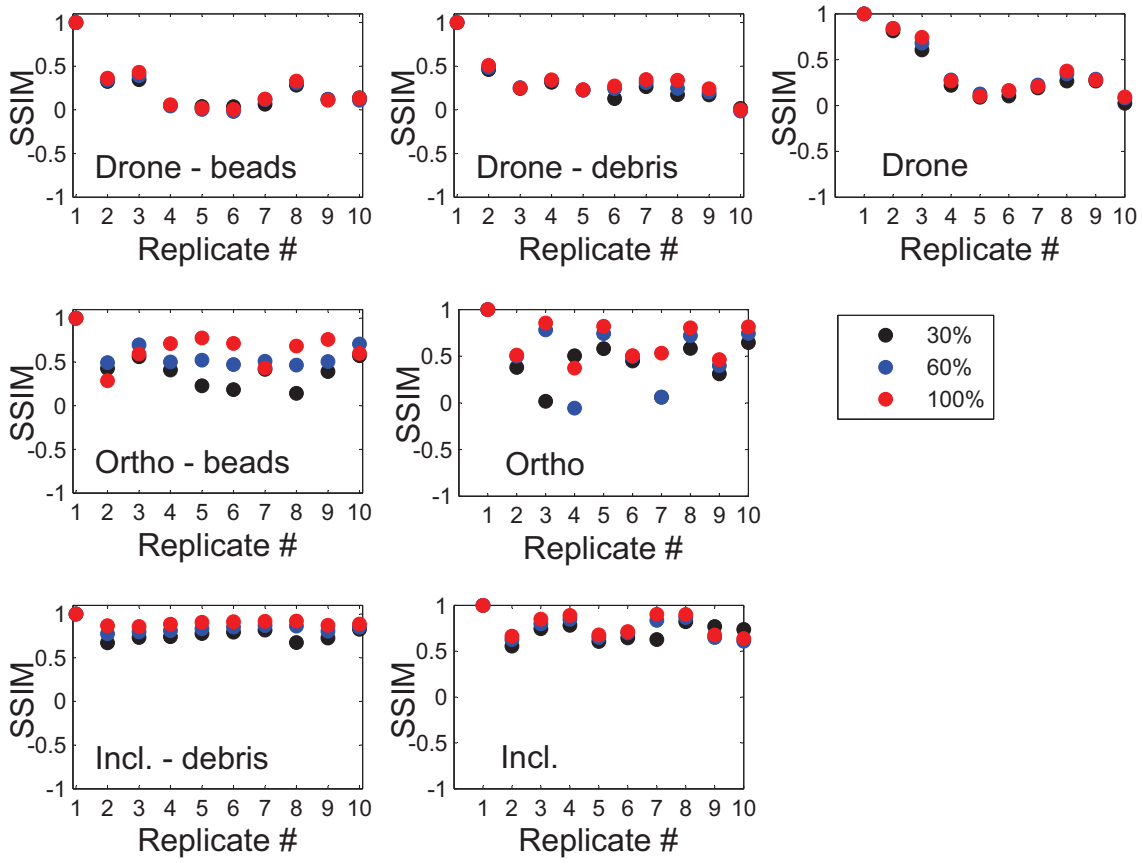

Figure 3.4: Artificial channel: SSIM values for each experimental condition. In the top row, SSIM values are displayed for drone data (Drone) in case of beads, debris, and without tracers. In the central row, SSIM values are reported for the fixed-ortho configuration (Ortho) in case of beads and without tracers. In the bottom row, SSIM values are showed for the fixed-inclined configuration (Incl.) in case of debris and without tracers. For each replicate, SSIM values are computed considering 30% (black markers), 60% (blue markers), and 100% (red markers) of the image sequences.

However, only the ortho-beads data show weakly statistically significant variability ($p = 0.0441$) with respect to the observation time length. High standard deviation is found in the drone-debris data. Such behavior may be attributed to the fact that the large quantities of debris deployed in the stream require longer observations (average observation time equal to 1.1 s in Table 2) with respect to alternative settings. Notably, such behavior is not observed in case of the inclined configuration, whereby long observation times do not correspond to high standard deviations in maximum velocities.

Among all the considered configurations with tracers, median values from inclined-debris data are found to be the lowest. Further, medians obtained in the absence of tracers (that is, drone, ortho, and incl. in Figure 3.5) tend to be lower than values computed on videos with tracers, with the only exception of the drone-debris configuration. The standard deviations of the maxima also tend to decrease in the absence of added material. Analysis of variance with respect to tracers results in generally statistically significant variability. Specifically, drone data variability is weakly statistically significant when 30% ($p = 0.0225$) and 60% ($p = 0.0471$) of the image sequences are considered. Variability of data from the fixed-ortho configuration is found strongly statistically significant when 30% ($p = 5.6 \times 10^{-5}$) and 100% ($p = 4.2 \times 10^{-}4$) of the image sequences are considered, and weakly statistically significant when 60% ($p = 0.011$) of the image sequences are analyzed. In addition, the fixed-ortho configuration is the most highly affected by the absence of tracing material, with medians for the ortho data equal to $75-81\%$ the corresponding values obtained in case of bead deployment (ortho-beads in Figure 3.5). The variability of data from the inclined configuration with respect to tracers is consistently strongly statistically significant ($p = 7 \times 10^{-6}$, 0.0042, and 1.5×10^{-4} when 30%, 60%, and 100% of the image sequences are analyzed, respectively).

3.1.5 Cross-sectional surface profile reconstruction

Range values of three cross-sectional profiles lying in the shared subarea of the stream are reported in Figure 3.6. On average, ranges pertaining to drone data are higher than values from the fixed configurations. Specifically, average values of 2.05 m/s and 1.76 m/s are found for the drone-beads and drone-debris data, respectively, against 1.56 m/s and 1.65 m/s for the ortho-beads and inclined-debris configurations, respectively. On the other hand, all configurations with tracers present similar standard deviations (minimum equal to 0.24 m/s in case of drone-bead data and 100% of the image sequence, and maximum equal to 0.37 m/s in case of drone-debris data and 100% of the image sequence). Similar to maximum velocity values, in the absence of

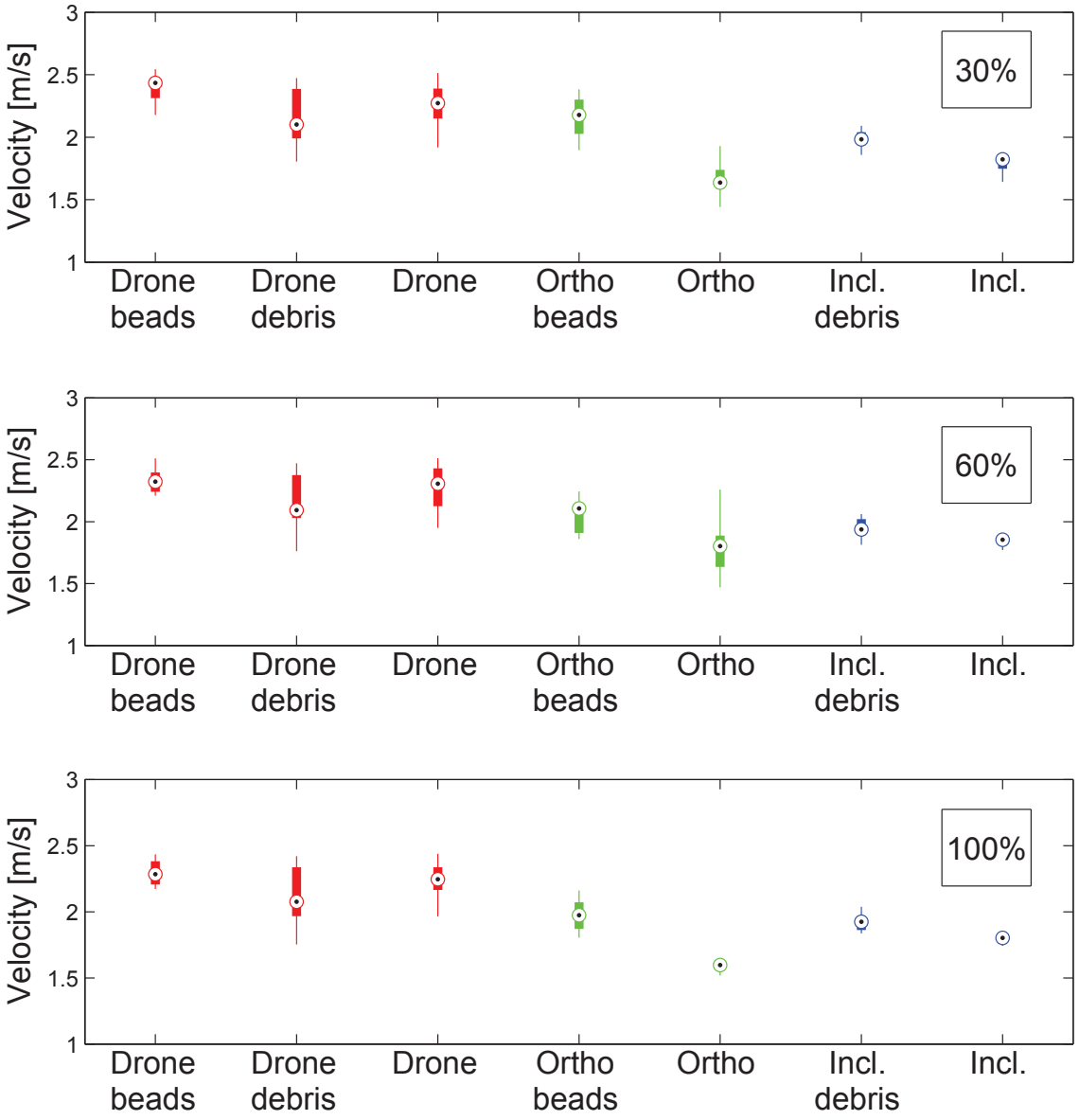

Figure 3.5: Artificial channel: maximum velocity values in the shared subarea for each experimental condition. Markers indicate medians computed over the experimental replicates. The edges of the box indicate the 25th and 75th percentiles, and the whiskers extend to extreme data points that are not outliers. For each replicate, maximum velocity values are computed considering 30% (top graph), 60% (central graph), and 100% (bottom graph) of the image sequences.

tracers, median values tend to be lower, with the only exception of the drone-debris configuration. On the other hand, the standard deviation from data without tracers sensibly increases with respect to experiments with tracers (see, for instance, data for the inclined configuration without tracers in Figure 3.6).

The variability of all data sets with respect to the observation time length is not found statistically significant. However, strong statistical significance is found for drone data with regards to tracers ($p = 0.0069$, 0.0048, and 0.0015 when 30%, 60%, and 100% of the image sequences were analyzed). Similarly, strong statistical significance is observed for the fixed configurations with respect to tracers. Specifically, p values for data from the fixed-ortho configuration are equal to 9.6×10^{-9}, 5.3×10^{-9}, and 2.3×10^{-9} when 30%, 60%, and 100% of the image sequences are considered, respectively. For the inclined configuration, p values are equal to 0.0021, 2.1×10^{-4}, and 0.002 when 30%, 60%, and 100% of the image sequences are analyzed, respectively.

3.2 Diverging segment

Time-averaged surface flow velocity maps for the diverging segment of the stream are presented in Figure 3.7, where the profiles for three representative cross-sections in the shared subarea are also illustrated. In this location, the water level is very shallow and the appearance of the stream bed is rather bright. In addition, challenges in seeding the large water surface and directly incident sunlight contribute to reduce the visibility of tracers in captured images. As depicted in Figure 3.7, these factors are particularly detrimental for the generation of accurate velocity maps. For instance, in Figure 3.7(a), a large number of low velocity nodes are found, whereas higher values are only exhibited in the shared subarea.

3.2.1 Sensitivity to tracers' transit

In the diverging segment, experiments with the drone are performed at a greater height from the ground to capture a more extended field of view, see Section 2.3. The lower quality of images taken from such a height is evident in Figure 3.8, where most of the replicates in the drone configuration (top row) present more than 60% of low velocity nodes out of the total number. Conversely, in replicates from the fixed-inclined configuration (bottom row), low velocity nodes are a meagre percentage. Without tracers, the number of low velocity nodes either remains considerable, see the drone configuration, or slightly increases, see the fixed-inclined configuration. None of the configurations presents statistically significant variability with respect to the observation time length. However, the variability of data from the inclined

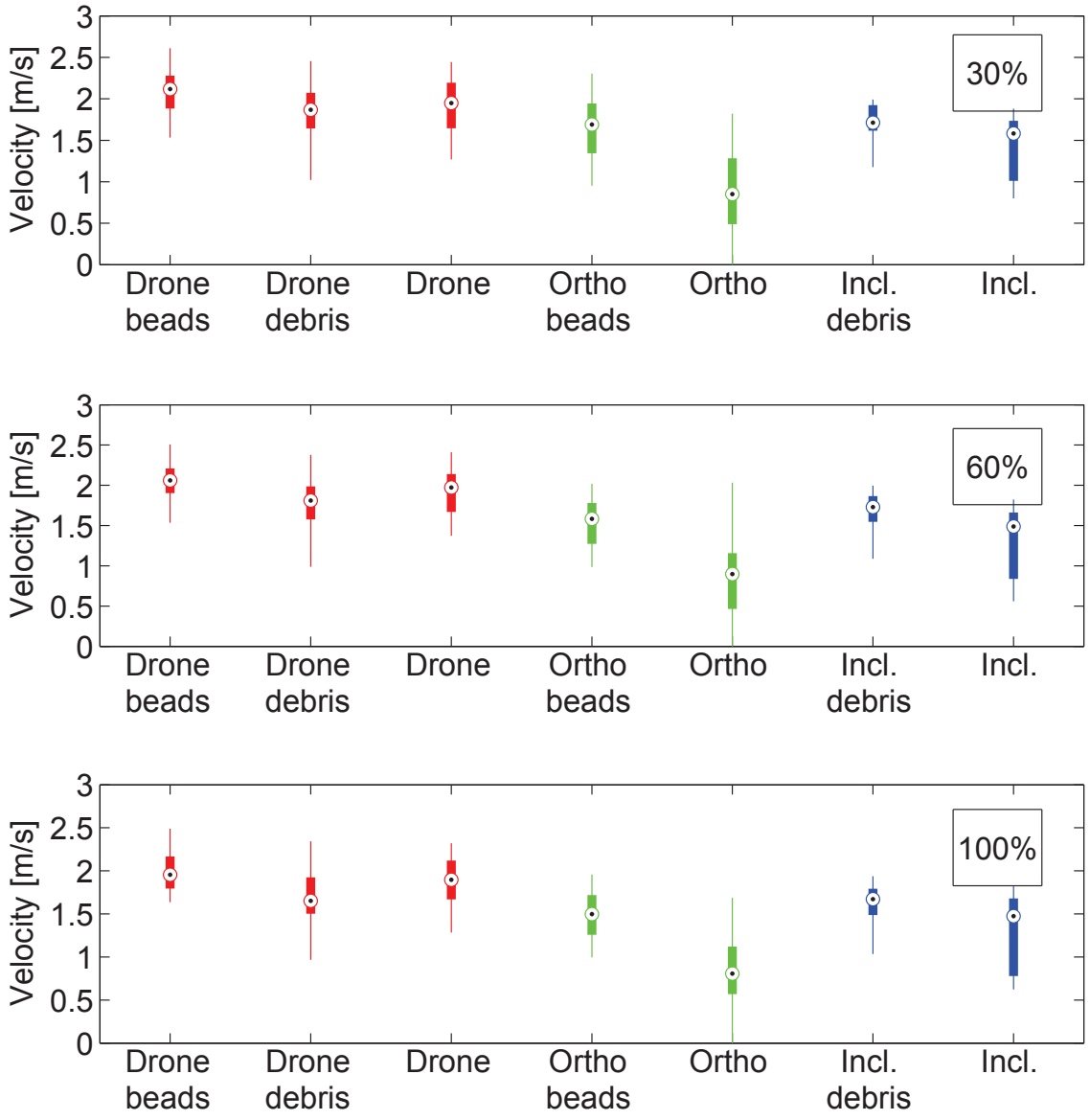

Figure 3.6: Artificial channel: velocity range values for cross-sections in the shared subarea for each experimental condition. Markers indicate medians computed over the experimental replicates. The edges of the box indicate the 25th and 75th percentiles, and the whiskers extend to extreme data points that are not outliers. For each replicate, velocity range values are computed considering 30% (top graph), 60% (central graph), and 100% (bottom graph) of the image sequences.

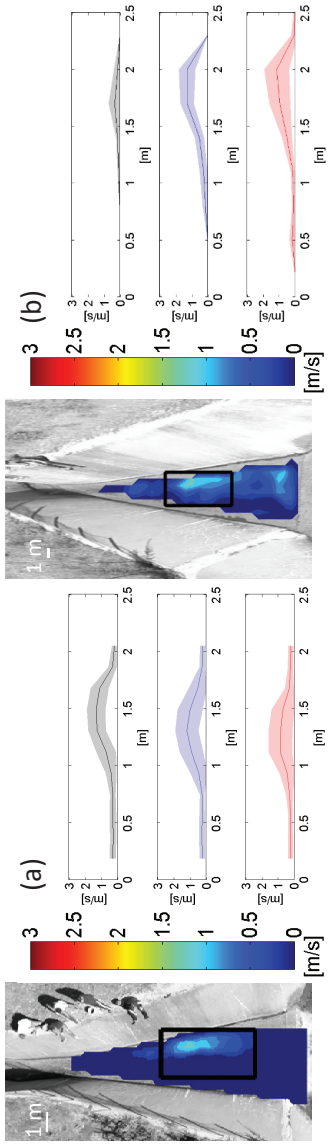

Figure 3.7: Representative surface flow observations for experiments conducted in the diverging segment. (a) Time-averaged surface flow velocity map and cross-sectional profiles generated from drone data in case of natural debris as tracer. (b) Time-averaged surface flow velocity map and cross-sectional profiles generated from data captured through the fixed-inclined configuration in case of natural debris as tracer.

configuration with respect to tracers is strongly statistically significant ($p = 9.6 \times 10^{-7}$, 8.3×10^{-6}, and 4.1×10^{-5} when 30%, 60%, and 100% of the image sequences were analyzed, respectively). A behavior similar to observations in the artificial channel is also found for the index D, not reported for the diverging segment, whereby the drone configuration presents percentages of negative nodes ranging from 57% to 66%.

3.2.2 Experiment repeatability

Similar to Figure 3.4, in Figure 3.9, time-averaged velocity maps are consistent among different replicates. In particular, maps from the fixed-inclined configuration (bottom row) present values of the SSIM proximal to one. In the absence of tracers, drone data show a dependence on the observation time length, whereas data from the fixed configuration are mostly identical to one. However, data sets variabilities are not found statistically significant with respect to the observation time length nor with regards to tracers.

3.2.3 Measurement accuracy

In Figure 3.10, the maximum velocity values estimated in the shared subarea and over the selected image sequences are reported. Median velocities are slightly higher in drone-debris data. Further, median values tend to decrease with longer observation times for both configurations with tracers (drone-debris and inclined-debris). With regards to standard deviations, similar values are also obtained in both configurations with tracers. The absence of tracers strongly impacts both sets of data, with lower values observed in the drone configuration. None of the data sets exhibits statistically significant variability with respect to the observation time length. However, the variability with respect to tracers is strongly statistically significant for both the drone and the fixed configuration ($p = 7.7 \times 10^{-7}$, 3.4×10^{-6}, and 1.6×10^{-6} when 30%, 60%, and 100% of the image sequences are analyzed, respectively, for the drone data, and $p = 4.2 \times 10^{-4}$, 1.1×10^{-4}, and 4.7×10^{-5} when 30%, 60%, and 100% of the image sequences are analyzed, respectively, for the fixed inclined data).

3.2.4 Cross-sectional surface profile reconstruction

In Figure 3.11, range values for three representative cross-sectional profiles in the shared subarea are presented. Both configurations present high variability (standard deviation from a minimum of 0.24 m/s to a maximum of 0.38 m/s for the drone-debris

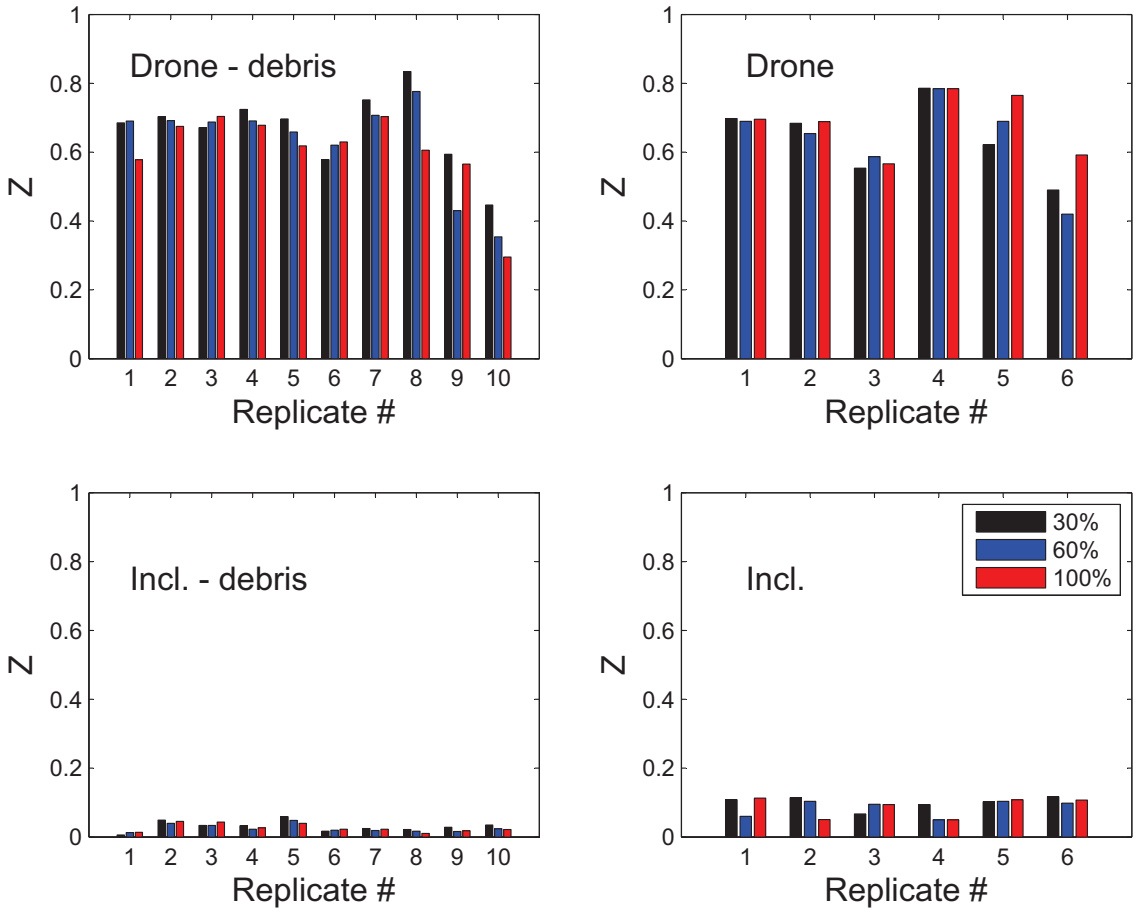

Figure 3.8: Diverging segment: Z values for each experimental condition. In the top row, drone data (Drone) are reported in case of debris and without tracers. In the bottom row, data are showed for the fixed-inclined configuration (Incl.) in case of debris and without tracers. For each replicate, Z values are computed considering 30% (black bars), 60% (blue bars), and 100% (red bars) of the image sequences.

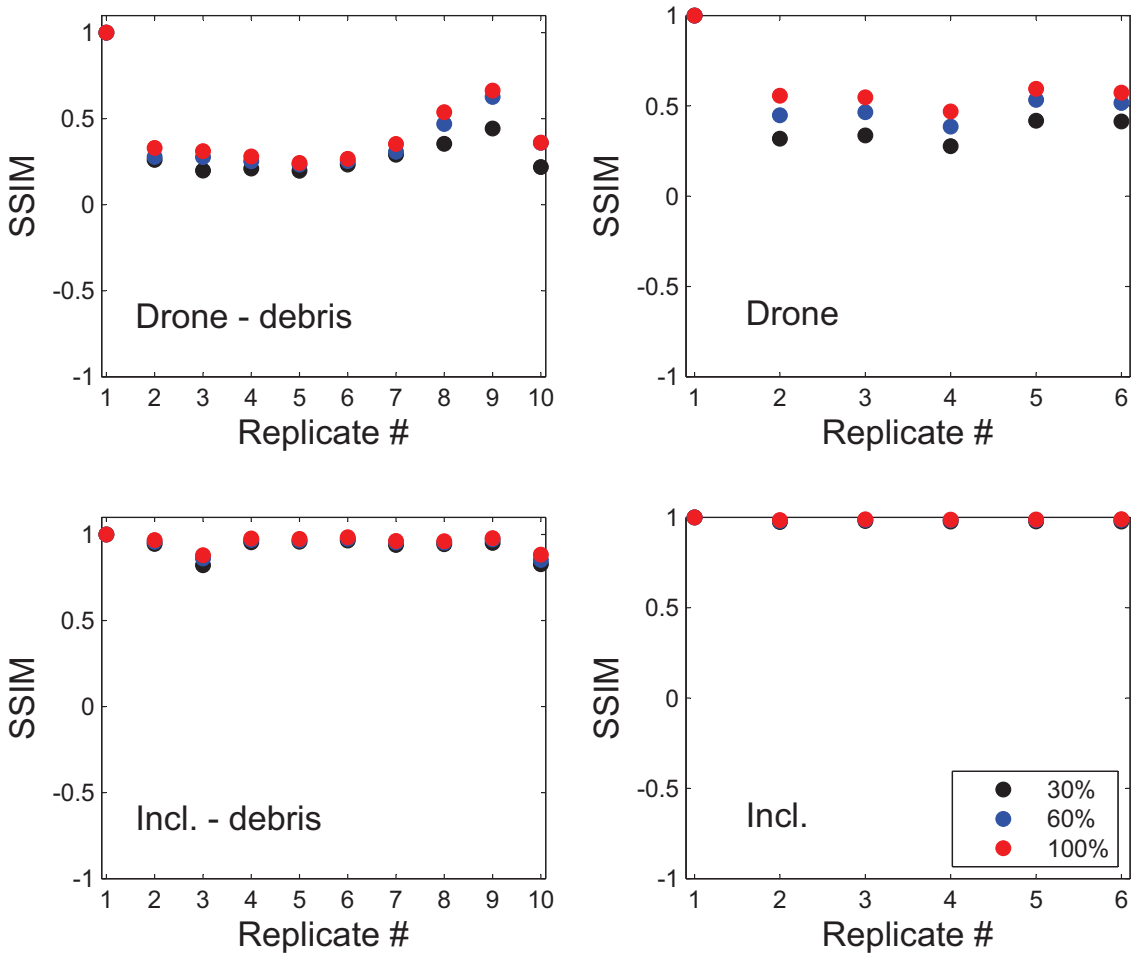

Figure 3.9: Diverging segment: SSIM values for each experimental condition. In the top row, SSIM values are displayed for drone data (Drone) in case of debris and without tracers. In the bottom row, SSIM values are showed for the fixed-inclined configuration (Incl.) in case of debris and without tracers. For each replicate, SSIM values are computed considering 30% (black markers), 60% (blue markers), and 100% (red markers) of the image sequences.

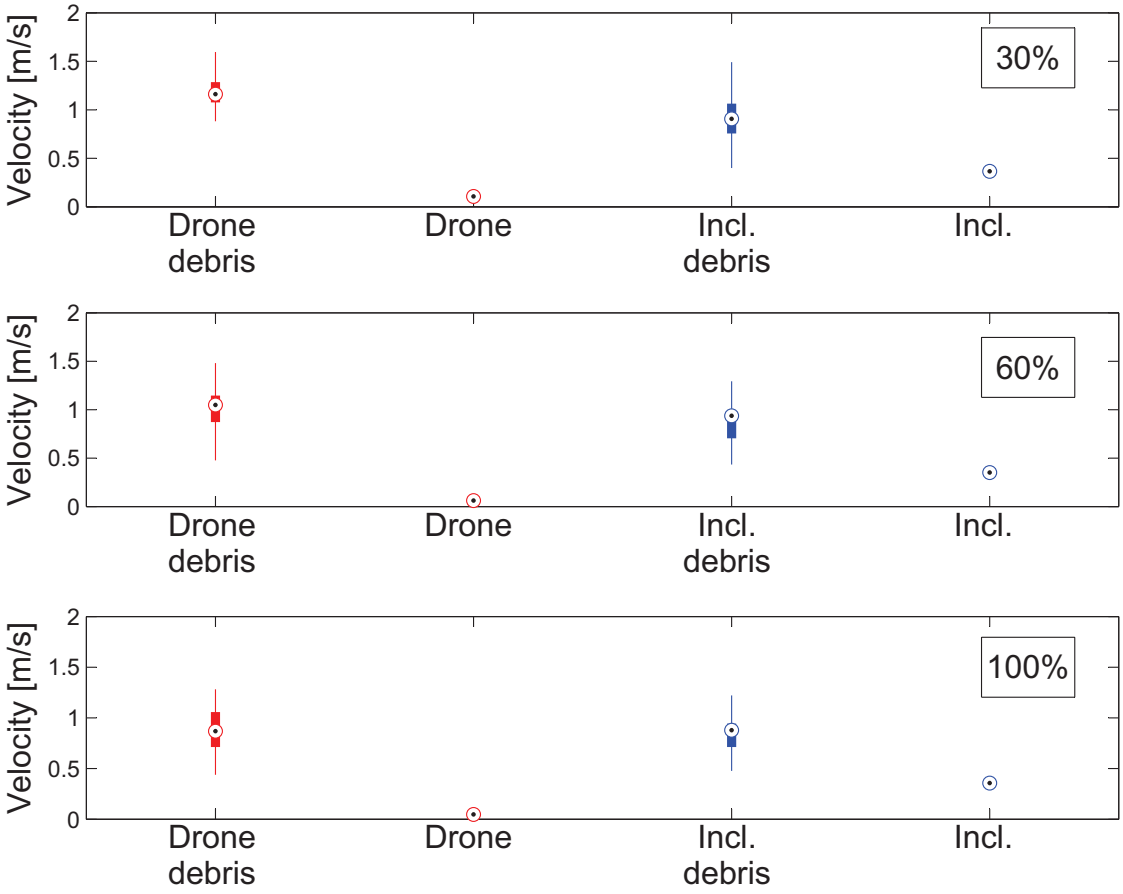

Figure 3.10: Diverging segment: maximum velocity values in the shared subarea for each experimental condition. Markers indicate medians computed over the experimental replicates. The edges of the box indicate the 25th and 75th percentiles, and the whiskers extend to extreme data points that are not outliers. For each replicate, maximum velocity values are computed considering 30% (top graph), 60% (central graph), and 100% (bottom graph) of the image sequences.

data, and from a minimum of 0.35 m/s to a maximum of 0.37 m/s for the inclined-debris data). In the inclined-debris data, the average range is equal to 0.94 m/s, whereas the average range is 0.75 m/s for the drone-debris data. Interestingly, the variability of drone-debris data is strongly statistically significant ($p = 0.0089$) with respect to the observation time length, whereas the variability of inclined-debris data with regards to time is weakly statistically significant ($p = 0.0225$). Similar to maximum velocities, all data are highly affected by the absence of added material (see, for instance, the low values for drone data in Figure 3.11). Specifically, for all observation time lengths, data from both configurations are strongly statistically significant ($p = 8.2 \times 10^{-11}$, 1.4×10^{-13}, and 1.9×10^{-12} when 30%, 60%, and 100% of the image sequences are analyzed, respectively, for the drone data, and $p = 6.1 \times 10^{-4}$, 3.6×10^{-7}, and 2.0×10^{-8} when 30%, 60%, and 100% of the image sequences are analyzed, respectively, for the fixed inclined data).

4 Discussion

As illustrated in Section 2, observations are achieved in challenging outdoor settings from a traditional LSPIV installation, a modified orthogonal LSPIV configuration, and an aerial platform. Despite practical challenges, spatially distributed surface velocity measurements are obtained at limited costs in areas that are generally difficult or impossible to access with alternative measurement techniques. Even if proximal, the selected experimental locations present radically different characteristics that impact image quality and, therefore, surface flow velocity measurements. On the one hand, the artificially channelled stream reach features high flow regime and a dark stream bed, and the high concrete banks block reflections due to direct sunlight. On the other hand, the diverging segment of the stream is characterized by very shallow depths and incident sunlight, that severely affects tracer visibility. An overview of the experimental results is presented in Figure 4.1.

Based on Figures 3.2 and 3.8, maps obtained from drone data tend to present larger regions at low velocity. In case of the diverging segment of the stream and the drone configuration, the number of low velocity nodes is very significant. While this may suggest that the drone elevation from the water surface is very high, this result also hints at the challenging experimental conditions and, in particular, at the severe illumination settings that limit tracer visibility. In the same location, in case of the fixed-inclined configuration, low velocities nodes are very few and, according to Z values, experimental conditions can not be deemed critical. In the absence of tracing material, see Figure 3.2 for the artificial channel, the number of low velocity nodes increases in all configurations but it is much more appreciable

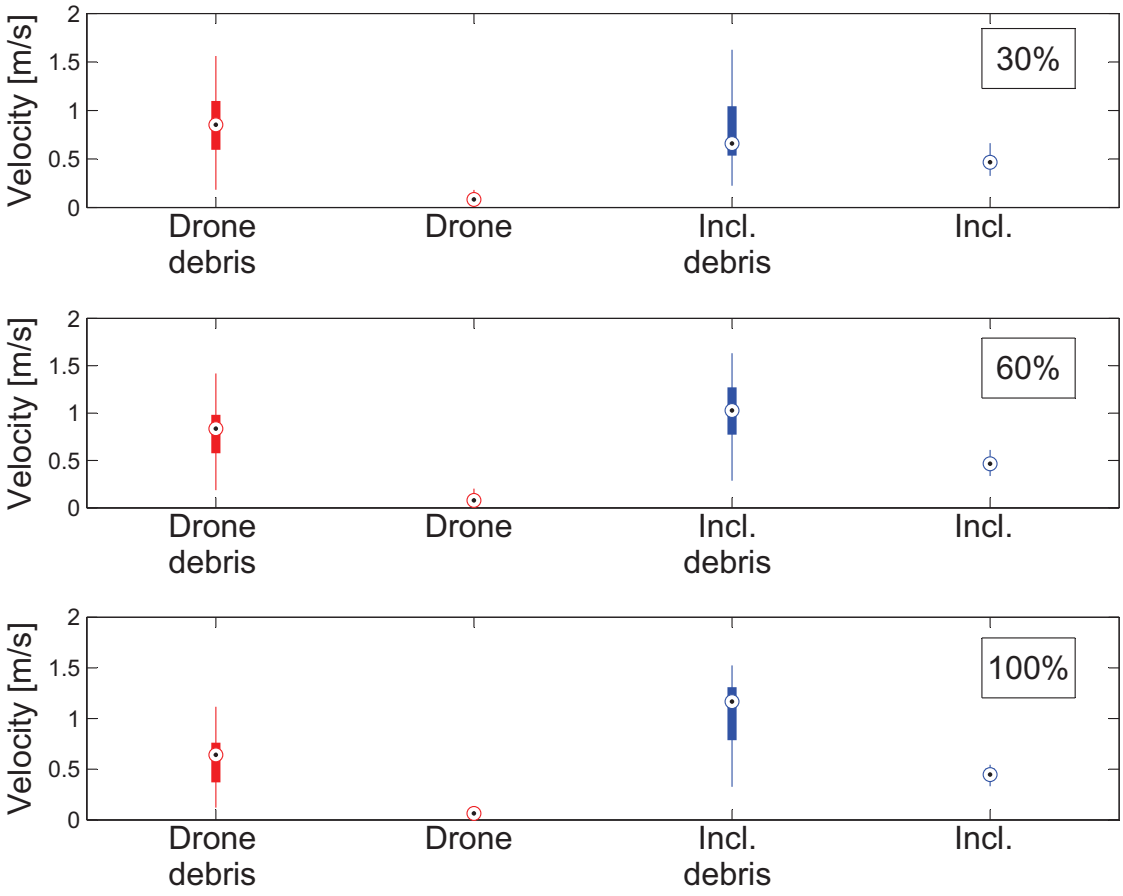

Figure 3.11: Diverging segment: velocity range values for cross-sections in the shared subarea for each experimental condition. Markers indicate medians computed over the experimental replicates. The edges of the box indicate the 25th and 75th percentiles, and the whiskers extend to extreme data points that are not outliers. For each replicate, velocity range values are computed considering 30% (top graph), 60% (central graph), and 100% (bottom graph) of the image sequences.

Artificial Channel	Z	D	SSIM	Max	Range
Drone	- Higher values for beads data - Significance to tracers	- No significance to tracers nor obs. time	- Generally lower values than other configurations - No significance to tracers nor obs. time	- Generally higher values than other configurations - Higher values with bead data - Significance to tracers	- Generally higher values than other configurations - Higher values with bead data - Significance to tracers
Ortho	- Significance to tracers	n.a.	- No significance to tracers nor obs. time	- Significance to tracers and obs. time	- Significance to tracers
Inclined	- No significance to tracers nor obs. time	n.a.	- Generally higher values than other configurations - Significance to obs. time and tracers	- Significance to tracers	- Significance to tracers
Diverging Segment	**Z**	**D**	**SSIM**	**Max**	**Range**
Drone	- Generally higher values than other configurations - No significance to tracers nor obs. time	- No significance to tracers nor obs. time	- No significance to tracers nor obs. time	- Generally higher values than other configurations - Significance to tracers	- Significance to tracers and obs. time
Inclined	- Significance to tracers	n.a.	- Generally higher values than other configurations - No significance to tracers nor obs. time	- Significance to tracers	- Generally higher values than other configurations - Significance to tracers and obs. time

Figure 4.1: Synoptic table of the experimental results for experiments in the artificial channel and the diverging segment of the stream. The acronym n.a. stands for not applicable.

in case of the drone. Therefore, a change in the experimental conditions is more clearly captured from the aerial rather than the fixed setups. This suggests that the aerial configuration is more sensitive to the transit of tracers. However, in the diverging segment in Figure 3.8, the variability to tracers of data from the fixed configuration is statistically significant. With regards to the stability of the aerial platform, Figure 3.3 shows that the number of velocity vectors opposing the flow is around 20% of the total nodes. Since this result is not affected by different types of tracers, it could be addressed by either designing more sophisticated techniques for drone-vibration removal in images or improving the onboard GPS.

As presented in Figures 3.4 and 3.9, generated maps are generally repeatable and the SSIM is constant among different replicates. Specifically, the SSIM index should capture the similarity in the structure of the maps (that is, for instance, if high velocity regions are found at consistent locations among different experimental replicates). Given the stationarity of the observed phenomena (experiments are performed on the same day and at few hours difference), this finding demonstrates the repeatability of the measurements. It is commented that in the computation of the SSIM index, the first time-averaged map is used as reference and, therefore, SSIM$= 1$ for the first experimental replicate. Interestingly, maps from drone data are slightly affected by the observation time length, whereas the similarity increases for longer experiments in case of fixed configurations. In data for the fixed-ortho configuration Figure 3.4, the variability is higher than in the alternative configurations. This behavior can be attributed to the fact that this configuration captures the smallest field of view and, therefore, it is the most highly influenced by small variations in illumination and reflections. On the other hand, in data relative to the fixed-inclined configuration in Figure 3.4, the similarity among different replicates is very high and probably due to the fact that a large field of view is captured at a relatively low resolution. This finding hints that accurate drone-based measurements may be collected through short-time observations. Further, different from alternative configurations, the medium distance of the aerial camera from the the study area enables to capture tracers' transit while guaranteeing experiment repeatability.

Figures 3.5 and 3.10 show that drone-based estimates tend to be higher and, therefore, closer to actual velocities, than estimates from fixed configurations. In case of the artificially channelled stream, measurements from the current meter result in an average velocity of $2.54\,\mathrm{m/s}$ in the center of the stream (corresponding to the location of the shared subarea). While lower velocity is expected on the stream surface due to wind effects, all LSPIV estimates are lower than benchmark measurements, thus suggesting that optical measurements can be severely impacted by illumination and tracers' visibility. However, in this work, experiments are per-

formed during an entire day and, therefore, in case of varying illumination conditions. Hence, it is expected that improvements in seeding the water surface and the continuous deployment of tracers may lead to more accurate velocity estimates. With regards to the diverging segment, benchmark measurements from manual tracking result in average velocities equal to $1.5 - 1.8\,\mathrm{m/s}$, approximately 60% higher than medians obtained from drone-debris data considering 30% of the image sequences, see Figure 3.10. Therefore, in this location, tracer visibility also plays a crucial role and it highly affects data from the fixed-inclined configuration. These results show that optical measurements still mandate considerable improvement for accurate hydrological measurements; however, the medium-ranged fields of view captured with aerial platform offer diffused rather direct illumination, thus leading to flow velocity estimates closer to actual values.

The effect of the absence of tracers results in different scenarios in the two locations. In the artificially channelled stream, see Figure 3.5, maximum velocity estimates from the drone without tracers are similar to drone-beads data. On the other hand, the fixed-ortho configuration is highly affected by the absence of tracers and maximum velocities considerably decrease. With regards to the fixed-inclined configuration, maximum velocities are also impacted. In the diverging segment, see Figure 3.10, drone-based estimates tend to be slightly higher than measurement from the fixed configuration for all the considered observation time lengths. In addition, both configurations, and in particular the drone, are highly impacted by the absence of tracers, regardless the length of the image sequences.

In the artificially channelled location, drone-based ranges are on average higher than in case of fixed configurations, see Figure 3.6. The lowest values are obtained in case of the fixed-ortho configuration, whereas highest variability is found for the drone-debris data. In the absence of tracers, the fixed-ortho configuration is very highly affected. In the diverging segment, see Figure 3.11, average range values from drone data are lower than average data from the inclined-debris configuration. In the absence of tracers, maps from the drone result in ranges proximal to zero, see Figure 3.11.

The influence of the observation time length also leads to different results for the analyzed parameters. In particular, indices Z, D, and the range are not highly affected by the time length of the experiment. Conversely, the fixed configurations demonstrate a dependence, even if not always statistically significant, on the length of the observations in the SSIM index computed in the artificially channelled stream, see Figure 3.4. Drone-based SSIM values are instead unaffected by time, with the exception of experiments without tracers in Figure 3.9. Maximum velocities computed for all configurations are affected, though not statistically significantly, by the

observation time length. Specifically, mean values and standard deviations tend to decrease with longer image sequences. This finding suggests that longer observations do not necessarily lead to more accurate surface flow observations, as regions without visible tracers are considered in the time-averaging process.

Finally, the effect of the different type of tracer is evaluated in the artificially channelled location in experiments performed with the drone configuration. The index Z and the maximum velocities in the subarea result sensitive to different tracers, whereby a smaller number of low velocity nodes and lower maximum velocities are found for debris. This finding suggests that the good visibility of the beads may lead to accurate velocity estimations (high maxima). Finally, while all configurations are impacted by the absence of tracers, more relevant differences are found in drone-based data, whereas the fixed-inclined configuration is the least effected.

Based on the high sensitivity to the transit of tracers and on the fact that maximum velocity estimates are closer to benchmark values, airborne observations are found promising for hydrological surface flow measurements. Notably, we remark that a low-cost ready-to-fly aerial platform and a sport camera are here utilized for surface flow measurements. Future technological advancements are expected to highly improve the platform stability and image quality, thus offering accurate measurements at competitive costs. We also emphasize that airborne observations offer several practical advantages with respect to traditional fixed implementations. Indeed, several acquisition parameters can be adjusted to improve data quality. Such parameters include: the platform's elevation, the size of the field of view with respect to image resolution, and the selection of the measurement area. With regards to the study area, we expect airborne observations to be beneficial for diverse compartments of hydrological catchments, spanning from ephemeral rills to floodplain environments, where traditional ground-measurement systems are impractical. However, the slope of the water surface should be accounted for in case of observations over rather extended areas.

5 Conclusions

In this work, an assessment of drone-based LSPIV is presented by comparing experiments executed with a commercial drone to measurements with fixed LSPIV configurations and independent benchmark surface flow velocity measurements. Experiments are conducted at two different locations on a mountainous stream in the Italian Alps using high-visibility beads and debris as tracers. To estimate the performance of the experimental configurations, LSPIV analyses are also performed on videos of the water surface recorded without any added tracing material. The tested

locations present radically different settings, whereby shadowy surfaces and high flow rates are observed in the artificially channelled stream reach and direct sunlight and lower velocities are found in the diverging stream reach.

Based on experimental findings, drone-based data lead to maps comparable to LSPIV traditional configurations. However, experiments executed with the drone result in maximum velocities closer to benchmark values as compared to the alternative LSPIV configurations. Drone-based data are sensitive to the presence of tracing material and the different type of tracer. On the other hand, traditional fixed LSPIV implementations (fixed-inclined) are not highly influenced by the observation time length and the absence of tracers. The modified fixed configuration (fixed-ortho) captures smaller fields of view and, therefore, presents higher variability with regards to varying experimental conditions.

Experimental findings support the use of drones for hydrological surface flow measurements. Nonetheless, the following factors should be considered to obtain accurate results: i) height of the vehicle with respect to the water surface: larger heights may be detrimental for measurement accuracy due to decreased visibility; ii) illumination conditions: direct sunlight may decrease the visibility of tracing material; iii) presence of tracers: the effect of homogeneously distributed floaters highly improves the generation of velocity maps. An important issue that should be addressed in the future entails the stability of the drone. Advanced image analysis and/or integration of high-precision GPS in the system should be explored to mitigate limitations in the drone's hovering capability, that may result in velocity vectors in the opposite direction of the flow.

Traditional fixed-inclined LSPIV implementations also present several issues. While not sensibly affected by the time length of the observation, measurements are consistently underestimated with respect to drone-based data and benchmark values. In addition, the low sensitivity of the methodology to the type or absence of tracers in the traditional fixed-inclined configurations raises several questions on the validity of the technique in challenging settings. On the one hand, selecting low image resolutions with respect to the actual fields of view may help mitigating the scarcity of tracers. On the other hand, the high distance of the apparatus from the water surface also results in lower velocity values and less accurate maps.

Besides ascertaining the potential of aerial platforms for noninvasive surface flow measurements, experimental findings point out several inherent limitations in LSPIV practice. Specifically, the sensitivity of the approach to the quantity and spatial distribution of tracing material severely constrains the applicability of the methodology in natural environments. According to results presented in this work, all configurations suffer from tracer-related factors, especially in case of the adversely illuminated

water surface in the diverging segment of the stream. Toward future enhancements of remote surface flow observations, alternative algorithms, such as particle tracking velocimetry, should be taken into account to determine the flow velocity field in natural water bodies.

Acknowledgements

This work was supported by the Ministero degli Affari Esteri project 2015 Italy-USA PGR00175, by the American Geophysical Union Horton (Hydrology) Research Grant for Ph.D. students, and by the Honors Center of Italian Universities. The authors gratefully thank Mr. Gabriele Mocio and members of the Mechanical Engineering for Hydrology and Water Science Laboratory at University of Tuscia for support and help with the experiments.

References

Adrian, R.J., 1991. Particle-imaging techniques for experimental fluid-mechanics. Annual Review of Fluid Mechanics 23, 261–304.

Adrian, R.J., 2005. Twenty years of particle image velocimetry. Experiments in Fluids 39, 159 –169.

Bechle, A., Wu, C., Liu, W., Kimura, N., 2012. Development and application of an automated river-estuary discharge imaging system. Journal of Hydraulic Engineering 138, 327–339.

Bradley, A.A., Kruger, A., Meselhe, E.A., Muste, M.V.I., 2002. Flow measurement in streams using video imagery. Water Resources Research 38, 1–8.

Buchanan, T.J., Somers, W.P., 1969. Discharge measurements at gaging stations: U.S. geological survey techniques of water-resources investigations. Technical Report. U.S. Geological Survey.

Cohen, J., 2007. Drone spy plane helps fight California fires. Science 318, 727.

Creutin, J.D., Muste, M., Bradley, A.A., Kim, S.C., Kruger, A., 2003. River gauging using PIV techniques: a proof of concept experiment on the Iowa River. Journal of Hydrology 277, 182–194.

DJI, 2014. http://www.dji.com/.

638 Eltner, A., Baumgart, P., Maas, H.G., Faust, D., 2014. Multi-temporal UAV data
639 for automatic measurement of rill and interrill erosion on loess soil. Earth Surface
640 Processes and Landforms 40, 741–755. doi:10.1002/esp.3673.

641 Fujita, I., Muste, M., Kruger, A., 1997. Large-scale particle image velocimetry for
642 flow analysis in hydraulic engineering applications. Journal of Hydraulic Research
643 36, 397–414.

644 Gago, J., Douthe, C. anc Coopman, R.E., Gallego, P.P., Ribas-Carbo, M., Flexas,
645 J., Escalona, J., Medrano, H., 2015. UAVs challenge to assess water stress for
646 sustainable agriculture. Agricultural Water Management 153, 9–19.

647 Gui, L., 2013. EDPIV - Evaluation Software for Digital Particle Image Velocimetry.
648 http://lcgui.net.

649 Gunawan, B., Sun, X., Sterling, M., Shiono, K., Tsubaki, R., Rameshwaran, P.,
650 Knight, D., Chandler, J., Tang, X., Fujita, I., 2012. The application of LS-PIV
651 to a small irregular river for inbank and overbank flows. Flow Measurement and
652 Instrumentation 24, 1 – 12.

653 Hauet, A., Creutin, J.D., Belleudy, P., 2008. Sensitivity study of large-scale parti-
654 cle image velocimetry measurement of river discharge using numerical simulation.
655 Journal of Hydrology 349, 178 – 190.

656 Hauet, A., Muste, M., Ho, H.C., 2009. Digital mapping of riverine waterway hy-
657 drodynamic and geomorphic features. Earth Surface Processes and Landforms 34,
658 242–252.

659 Heimhuber, V., Hannemann, J.C., Rieger, W., 2015. Flood risk management in
660 remote and impoverished aarea – a case study of Onaville, Haiti. Water 7, 3832–
661 3860.

662 Hrachowitz, M., Savenije, H.H.G., Blöschl, G., McDonnell, J.J., Sivapalan, M.,
663 Pomeroy, J.W., Arheimer, B., Blume, T., Clark, M.P., Ehret, U., Fenicia, F.,
664 Freer, J.E., Gelfan, A., Gupta, H.V., Hughes, D.A., Hut, R.W., Montanari, A.,
665 Pande, S., Tetzlaff, D., Troch, P.A., Uhlenbrook, S., Wagener, T., Winsemius,
666 H.C., Woods, R.A., Zehe, E., Cudennec, C., 2013. A decade of predictions in
667 ungauged basins (PUB) a review. Hydrological Sciences Journal 58, 1198–1255.

668 Jodeau, M., Hauet, A., Paquier, A., Le Coz, J., Dramais, G., 2008. Application and
669 evaluation of LS-PIV technique for the monitoring of river surface velocities in
670 high flow conditions. Flow Measurement and Instrumentation 19, 117–127.

671 Kantoush, S.A., Schleiss, A.J., 2009. Channel formation during flushing of large
672 shallow reservoirs with different geometries. Environmental Technology 30, 855–
673 863.

674 Kantoush, S.A., Schleiss, A.J., Sumi, T., Murasaki, M., 2011. LSPIV implementation
675 for environmental flow in various laboratory and field cases. Journal of Hydro-
676 environment Research 5, 263 – 276.

677 Kim, Y., 2006. Uncertainty analysis for non-intrusive measurement of river discharge
678 using image velocimetry. Ph.D. thesis. Graduate College of the University of Iowa.

679 Kim, Y., Muste, M., Hauet, A., Krajewski, W.F., Kruger, A., Bradley, A., 2008.
680 Stream discharge using mobile large-scale particle image velocimetry: A proof of
681 concept. Water Resources Research 44, W09502.

682 Klemas, V.V., 2015. Coastal and environmental remote sensing from unmanned
683 aerial vehicles: an overview. Journal of Coastal Research 31, 1260–1267.

684 LeBoursicaud, R., Pénard, L., Hauet, A., Thollet, F., LeCoz, J., 2015. Gauging
685 extreme floods on YouTube: application of LSPIV to home movies for the post-
686 event determination of stream discharges. Hydrological Processes doi:10.1002/
687 hyp.10532.

688 Liu, C.C., Chen, P.L., Matsuo, T., Chen, C.Y., 2015. Rapidly responding to land-
689 slides and debris flow events using a low-cost unmanned aerial vehicle. Journal of
690 Applied Remote Sensing 9, 096016.

691 Luo, C., Nightingale, J., Asemota, E., Grecos, C., 2015. A UAV-cloud system for
692 disaster sensing applications, in: Vehicular Technology Conference (VTC Spring),
693 2015 IEEE 81st.

694 McDonnell, J.J., Sivapalan, M., Vaché, K., Dunn, S., Grant, G., Haggerty, R., Hinz,
695 C., Hooper, R., Kirchner, J., Roderick, M.L., Selker, J., Weiler, M., 2007. Moving
696 beyond heterogeneity and process complexity: a new vision for watershed hydrol-
697 ogy. Water Resources Research 43, W07301.

698 McGonigle, A.J.S., Aiuppa, A., Giudice, G., Tamburello, G., Hodson, A.J., Guerrieri,
699 S., 2008. Unmanned aerial vehicle measurements of volcanic carbon dioxide fluxes.
700 Gophysical Research Letters 35, L06303.

701 Muste, M., Fujita, I., Hauet, A., 2008. Large-scale particle image velocimetry for
702 measurements in riverine environments. Water Resources Research 44, W00D19.

703 Muste, M., Ho, H.C., Kim, D., 2011. Considerations on direct stream flow mea-
704 surements using video imagery: Outlook and research needs. Journal of Hydro-
705 environment Research 5, 289 – 300.

706 Pagano, C., Tauro, F., Grimaldi, S., Porfiri, M., 2014. Development and testest of an
707 unmanned aerial vehicle for large scale particle image velocimetry, in: ASME 2014
708 Dynamic Systems and Control Conference, San Antonio, Texas. p. V003T44A001.

709 Raffel, M., Willert, C.E., Wereley, S.T., Kompenhans, J., 2007. Particle Image
710 Velocimetry. A practical guide. Springer, New York.

711 Rippin, D.M., Pomfret, A., King, N., 2015. High resolution mapping of supra-glacial
712 drainage pathways reveals link between micro-channel drainage density, surface
713 roughness and surface reflectance. Earth Surface Processes and Landforms 40,
714 1279–1290.

715 Schiffman, R., 2014. Drones flying high as new tool for field biologists. Science 344,
716 459.

717 Shelley, L., Knuth, L., Cassano, J.J., 2014. Estimating sensible and latent heat
718 fluxes using the integral method from in situ aircraft measurements. Journal of
719 Atmospheric and Oceanic Technology 31, 1964–1981.

720 Smith, M.W., Vericat, D., 2015. From experimental plot to experimental landscapes:
721 topography, erosion and deposition in sub-humid badlands from Structure-from-
722 Motion photogrammetry. Earth Surface Processes and Landforms doi:10.1002/
723 esp.3747.

724 Tamminga, A., Hugenholtz, C., Eaton, B., Lapointe, M., 2015. Hyperspatial re-
725 mote sensing of channel reach morphology and hydraulic fish habitat using and
726 unmanned aerial vehicle (UAV): a first assessment in the context of river research
727 and management. River Research and Applications 31, 379–391.

728 Tauro, F., Grimaldi, S., Petroselli, A., Porfiri, M., 2012a. Fluorescent particle tracers
729 for surface flow measurements: a proof of concept in a natural stream. Water
730 Resources Research 48, W06528.

731 Tauro, F., Grimaldi, S., Petroselli, A., Rulli, M.C., Porfiri, M., 2012b. Fluorescent
732 particle tracers in surface hydrology: a proof of concept in a semi-natural hillslope.
733 Hydrology and Earth System Sciences 16, 2973–2983.

734 Tauro, F., Mocio, G., Rapiti, E., Grimaldi, S., Porfiri, M., 2012c. Assessment of
735 fluorescent particles for surface flow analysis. Sensors 12, 15827–15840.

736 Tauro, F., Pagano, C., Phamduy, P., Grimaldi, S., Porfiri, M., 2015a. Large scale
737 particle image velocimetry from an unmanned aerial vehicle. IEEE/ASME Trans-
738 actions on Mechatronics , Accepted for publication.

739 Tauro, F., Porfiri, M., Grimaldi, S., 2013a. Fluorescent eco-particles for surface flow
740 physics analysis. AIP Advances 3, 032108.

741 Tauro, F., Porfiri, M., Grimaldi, S., 2014. Orienting the camera and firing lasers to
742 enhance large scale particle image velocimetry for streamflow monitoring. Water
743 Resources Research 50, 7470–7483.

744 Tauro, F., Porfiri, M., Grimaldi, S., 2015b. Surface flow measurements from drones
745 Under review.

746 Tauro, F., Rapiti, E., Al-Sharab, J.F., Ubertini, L., Grimaldi, P., Porfiri, M., 2013b.
747 Characterization of eco-friendly fluorescent nanoparticle doped-tracers for envi-
748 ronmental sensing. Journal of Nanoparticle Research 15, 1884.

749 Tsubaki, R., Fujita, I., Tsutsumi, S., 2011. Measurement of the flood discharge of
750 a small-sized river using an existing digital video recording system. Journal of
751 Hydro-environment Research 5, 313–321.

752 Wang, Z., Bovik, A.C., Sheikh, H.R., Simoncelli, E.P., 2004. Image quality assess-
753 ment: from error visibility to structural similarity. IEEE Transactions on Image
754 Processing 13, 600–612.